Physica Medica 64 (2019) 45–53

Contents lists available at ScienceDirect

Physica Medica

journal homepage: www.elsevier.com/locate/ejmp

Original paper

Secondary radiation measurements for particle therapy applications: Charged secondaries produced by ^{16}O ion beams in a PMMA target at large angles

A. Rucinski[a,b], G. Traini[d,a,g,*], A. Baratto Roldan[k], G. Battistoni[c], M. De Simoni[d,a], Y. Dong[c,l], M. Fischetti[e,a], P.M. Fralliccardi[f,g], E. Gioscio[g], C. Mancini-Terracciano[a,d], M. Marafini[g,a], I. Mattei[c], R. Mirabelli[d,a,g], S. Muraro[i], A. Sarti[e,h,g], A. Schiavi[e,a], A. Sciubba[e,a,g], E. Solfaroli Camillocci[a,d,j], S.M. Valle[c,l], V. Patera[e,a,g]

[a] INFN – Sezione di Roma 1, Italy
[b] Institute of Nuclear Physics PAN, Krakow, Poland
[c] INFN – Sezione di Milano, Italy
[d] Dipartimento di Fisica, Sapienza Università di Roma, Roma, Italy
[e] Dipartimento di Scienze di Base e Applicate per Ingegneria, Sapienza Università di Roma, Roma, Italy
[f] Azienda Ospedaliero-Universitaria 'Ospedali Riuniti di Foggia', Foggia, Italy
[g] Museo Storico della Fisica e Centro Studi e Ricerche "E. Fermi", Roma, Italy
[h] Laboratori Nazionali di Frascati dell'INFN, Frascati, Italy
[i] INFN – Sezione di Pisa, Italy
[j] Scuola di Specializzazione in Fisica Medica, Sapienza Università di Roma, Roma, Italy
[k] Physics Department, University of Sevilla, Spain
[l] Dipartimento di Fisica, Università di Milano, Milano, Italy

ARTICLE INFO

Keywords:
Particle therapy
Oxygen beams
Range monitoring
Secondary radiation

ABSTRACT

Particle therapy is a therapy technique that exploits protons or light ions to irradiate tumor targets with high accuracy. Protons and ^{12}C ions are already used for irradiation in clinical routine, while new ions like ^{4}He and ^{16}O are currently being considered. Despite the indisputable physical and biological advantages of such ion beams, the planning of charged particle therapy treatments is challenged by range uncertainties, i.e. the uncertainty on the position of the maximal dose release (Bragg Peak – BP), during the treatment. To ensure correct 'in-treatment' dose deposition, range monitoring techniques, currently missing in light ion treatment techniques, are eagerly needed.

The results presented in this manuscript indicate that charged secondary particles, mainly protons, produced by an ^{16}O beam during target irradiation can be considered as candidates for ^{16}O beam range monitoring. Hereafter, we report on the first yield measurements of protons, deuterons and tritons produced in the interaction of an ^{16}O beam impinging on a PMMA target, as a function of detected energy and particle production position. Charged particles were detected at 90° and 60° with respect to incoming beam direction, and homogeneous and heterogeneous PMMA targets were used to probe the sensitivity of the technique to target inhomogeneities. The reported secondary particle yields provide essential information needed to assess the accuracy and resolution achievable in clinical conditions by range monitoring techniques based on secondary charged radiation.

1. Introduction

Charged particle therapy (PT) is presently used in more than 70 oncology centres worldwide, allowing patients to be treated with protons and carbon ions. In comparing PT to conventional radiotherapy using photons, the improvement in tumor control probability (TCP) can be viewed as a direct consequence of superior dose release selectivity, of higher relative biological effectiveness (RBE) and oxygen enhancement ratio (OER). These features significantly contribute to the reduction of both normal tissue exposure to radiation and complication

* Corresponding author.
E-mail address: giacomo.traini@roma1.infn.it (G. Traini).

https://doi.org/10.1016/j.ejmp.2019.06.001
Received 24 December 2018; Received in revised form 23 May 2019; Accepted 7 June 2019
Available online 24 June 2019

probability (normal tissue complication probability – NTCP) [6].

While for historical, technological and economical reasons particle therapy with protons is presently more widespread, also other ions, mostly ^{12}C ions, are nowadays investigated for therapy applications by oncologists and researchers [36,35,6].

The treatment plan optimization, and the related TCP and NTCP, can profit from the use of ^{4}He, ^{12}C, or ^{16}O beams, even using different ions for separate fractions within a treatment course [15,36,17,16,6]. On one hand, it has been recently shown that the high linear energy transfer (LET) of ^{16}O beams offers increased oxygen enhancement ratio (OER) with respect to lower Z ions, which could be effectively exploited to overcome hypoxia in the tumor region [33]. On the other hand, ^{16}O ions have to be accelerated to higher energies with respect to ^{12}C ions, and this represents a substantial technical and economical effort. Presently ^{16}O beams at therapeutic energies for deep-seated tumors are only available in a clinical environment at the Heidelberg ion beam therapy center (HIT), Germany.

Charged particle range uncertainty [11] is severely limiting the PT efficacy implying that displacements of the BP/dose distal fall-off positions, as predicted from the treatment planning software, with respect to the ones actually delivered during the treatment have to be properly handled. Safety margins have to be introduced in the treatment planning to account for many different factors, e.g. computed tomography (CT) scanner calibration, patient positioning uncertainties and anatomical variations occurring in the course of treatment. Range uncertainty is hence representing one of the greatest challenges in charged PT, and it is driving the development of particle range monitoring devices aiming to detect secondary radiation produced during the treatment. This radiation is typically generated inside the patient by nuclear interactions of the treatment beam, and can exit the body during irradiation [12]. The abundance of secondary radiation of different types, like back-to-back photon pairs from β^{+} emitters, prompt photons due to nuclear excitations, charged secondary particles and neutrons generated in nuclear fragmentation, depends on the flux and kind of primary particles used for irradiation [21] as well as on tumor location, composition and geometry of patient anatomy. Therefore, the optimal range monitoring method might differ for different ion types.

Currently, the most investigated proton therapy range monitoring technique is based on prompt-gamma (PG) detection, which was tested experimentally and clinically [14,29,38,39]. As it was already mentioned in Krimmer et al. [14] and Rucinski et al. [30], and discussed in Mattei et al. [21], the number of PG produced from ion beams with $Z > 1$ is smaller with respect to proton beams, while the uncorrelated background is increased, challenging the on-line verification of light ion range with the gamma detectors that are currently under development. Positron emission tomography (PET) can be an alternative to PG-based monitoring, exploiting the β^{+} emitters generated by the treatment beam. The post-irradiation PET verification is now mainly considered for protons [25,2,32,13,23,31] and it is facing several challenges due to high background, low signal rate and biological washout effects [24,4]. Moreover, in potential treatments with ^{16}O beams, one has to consider that the same biologically equivalent dose is obtained with less primary ions with respect to protons and carbon ions. Such primary flux decrease is not compensated by the increase in β^{+} emitters production, as known from the results already documented for ^{12}C ions [32,31]. The in-beam PET range verification of proton treatments was recently developed and tested clinically [34,26] showing promising results based on the successful detection of signal from short-lived ^{15}O emitters. The increasing abundance of charged secondary particles with increasing charge number Z of the primary ion makes them particularly suited for achieving the desired precision of on-line ion range verifications with ^{4}He, ^{12}C, or ^{16}O beams, providing the motivation to develop new range monitoring techniques, dedicated to such beams.

The measured emission profile can be exploited for PT range monitoring applications as it was suggested by it was suggested by [19], Agodi et al. [2], Agodi et al. [10], Gwosch et al. [9], Piersanti et al. [27], Mattei et al. [20], Rucinski et al. [30] and more extensively reviewed by Muraro et al. [22]. The production position of charged secondary particles has a distribution that depends on the primary beam range, but it is distorted when it is reconstructed outside the patient, due to the absorption along the exit path in the phantom/patient undergone by the fragments. Characterization and quantification of charged secondary radiation exiting the patient during the therapy, i.e. secondary particle yield, energy spectra and emission profiles are essential to design detectors that are suitable for beam range monitoring, and this information is also needed to assess the accuracy and resolution achievable by range monitoring techniques in clinical conditions. These quantities were not investigated experimentally before, and cannot be accurately predicted using Monte Carlo (MC) simulations.

This manuscript belongs to a paper series entitled *Secondary radiation measurements for particle therapy applications* aiming at characterizing the PG, charged particles and heavier fragments production when irradiating with ^{4}He, ^{12}C and ^{16}O beams. Hereafter are reported the secondary charged particles measurements performed using ^{16}O beams. These results are supplementary to the previous ones obtained studying ^{4}He and ^{12}C ion beams and documented in Rucinski et al. [30].

2. Materials and methods

2.1. Experimental set-up

In the presented work we studied secondary charged particles produced in the interaction of a primary ^{16}O beam with a polymethyl methacrylate (PMMA) target. The measurement were performed in the HIT experimental cave. Several targets with dimensions $5 \times 5 \times d_{PMMA}$ cm^3 were placed at the beam isocentre, varying the longitudinal length of PMMA target (d_{PMMA}) accordingly to the primary ^{16}O beam energy and range. In order to ease the forward fragmentation measurements [18], d_{PMMA} was adjusted to be about 2 cm longer with respect to the beam range for a given energy, in order to stop the beam in the PMMA target always at the same distance with respect to the fragment forward exit window. The reference frame is depicted in Fig. 1, and its origin is marked by a black spot within the PMMA. Table 1 lists the target configurations and beam conditions (beam energy, transverse size, range computed by means of a MC simulation) of

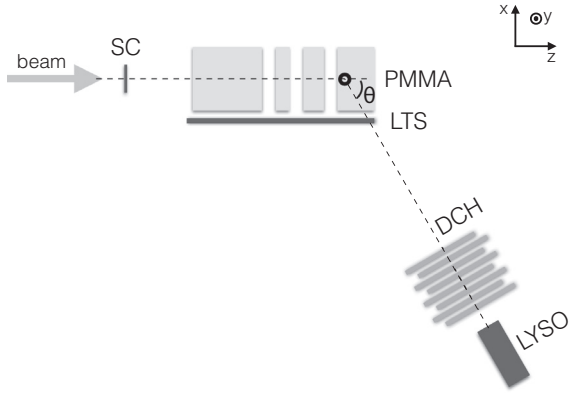

Fig. 1. The experimental set-up used for the emission measurements of charged secondary particles generated in a homogeneous target for a 60° detector configuration. Homogeneous and heterogeneous PMMA target configurations, as well as a 60° and 90° detector set-up mounted on a movable arm were used for the measurements reported in Table 1. SC was positioned 37 cm upstream of the PMMA target. The front faces of the detectors were positioned in the global reference frame at the following distance from the isocentre: LTS 8.0 cm, DCH: 50.5 cm (90°) and 55.0 cm (60°), LYSO: 73.5 cm (90°) and 78.0 cm (60°). The origin of the reference frame is placed about 2 cm before the distal edge of PMMA box. Figure is not to scale. The original figure was printed in Rucinski et al. [30].

Table 1
Target configurations and beam conditions used in the measurements. The columns are showing: the detector angle positioning with respect to the primary beam direction (θ), the energy of the ^{16}O beam, the FWHM of the transversal Gaussian shaped pencil beam (B_{FWHM}), the beam range in PMMA as computed from MC simulations (Range), the PMMA thickness along the beam direction (d_{PMMA}) and the total number of ions used in the measurements at the different angles (N_{ion}). The starred (*) values refer to the total number of collisions registered with the d_{PMMA} = 10.0 cm configuration obtained combining the homogeneous and heterogeneous target results.

Ion	θ	Energy (MeV/u)	B_{FWHM} (mm)	Range (cm)	d_{PMMA} (cm)	N_{ion} (90°/60°) × 10^9
^{16}O	90°–60°	210	4.6	5.8	7.7	1.9/ 1.2
		260	3.9	8.4	10.0*	2.2*/ 1.0
		300	3.6	10.7	12.7	2.4/ 1.4

the data set collected using ^{16}O beams. Homogeneous and heterogeneous PMMA target configurations, as well as different angular detector configurations (60° and 90°) were used in the measurements. The heterogeneous target consists of PMMA blocks (separated by air gaps) and have the same total length (d_{PMMA} = 10 cm) as the homogeneous target. Both targets were used to collect data using beams with energy 260 MeV/u.

The experimental set-up for the homogeneous target study, with the detector positioned at 60° with respect to the incoming beam direction, is sketched in Fig. 1. The detector acceptance, efficiency and particle identification were studied using FLUKA [7,5] MC simulations, in which the complete geometry of the experimental set-up was implemented. The MC simulation has been used to model the detector response to the incoming radiation in order to estimate its detection efficiency. No comparison with the MC prediction of fragment emission was performed, since the focus of the manuscript is on experimental results. The PMMA targets were assigned a density of 1.19 g·cm^{-3} and ionization potential of 74 eV in the MC simulations.

The detectors used for the charged particles measurement are: the 0.2 cm-thick start counter (SC) used for triggering purposes, a 0.1 cm-thick plastic scintillator (LTS) and a matrix of LYSO crystals, each of 1.5 × 1.5 × 12 cm^3 dimension, for time of flight (TOF) measurements, and a 21 cm-long drift chamber (DCH) used to reconstruct and track the charged particles, as sketched in Fig. 1. The SC provided also the number of impinging primary ions on the PMMA target. The secondary particles were detected by the LTS, DCH and LYSO detectors, aligned on a movable arm pointing towards the isocentre, and that could be placed at 60° or 90° with respect to primary beam direction.

The SC scintillator light was read-out by two Hamamatsu (H10580) Photomultiplier tubes (PMT), placed at two opposite sides of the scintillator, whereas the LYSO crystals matrix was read-out by a single EMI 9814B PMT. The DCH detector consisted of 12 wire layers oriented in alternating directions, i.e. six horizontal (x-z plane) and six vertical (y-z plane), used for the three dimensional reconstruction of particle tracks. More details regarding the DCH operation, signal read-out, signal discrimination and DCH performance, i.e. cell spatial resolution and efficiency as well as the reconstruction algorithms, can be found elsewhere [1,2,27]. The tracks were back-projected to compute the point of closest distance to the incoming beam axis, which was then used to build the charged secondary emission profile (see Section 3.3). The reconstructed tracks were also used to extrapolate the particle position in the LYSO detector, assigning each fragment to the appropriate LYSO crystal, with the same procedure described in Mattei et al. [21], Rucinski et al. [30]. The different light yield response of the LYSO crystals was equalized allowing a proper tuning of the particle identification cuts (see Section 2.2).

The time and charge electronic signals were read-out by the front-end, which was interfaced with a VME system connected to the data acquisition server, as it was described in detail elsewhere [27,20]. At the highest delivered beam rate of ~3 MHz, the global system trigger rate was in the 0.3–6 kHz range.

2.2. Data selection and particle identification

The events of interest have been selected using as trigger the coincidence within a 80 ns time window between the signal produced by the primary ions traversing the SC and the secondary particles that hit the LYSO.

The time difference between the signals produced by the charged secondary particles in the LTS and LYSO detectors was used to calculate the TOF and, consequently, the kinetic energy of the secondary particles (E^{Det}_{kin}, see Section 3.2) specific for each particle type (p,d,t). The energy released by the particles measured using the LYSO detector, i.e., the integrated pulse charge of the light detector coupled with the LYSO array, corrected for the light collection efficiency in individual pixels (LYSO charge), was used for particle identification (PID) purposes only. The charged particles were tracked by the DCH. A charged particle crossing the DCH is expected to produce in average one hit (in a single cell) in each transverse plane, resulting in a total number of N_{DCH} = 12 DCH cells fired. Fig. 2a and b show the number of particles selected requiring $N_{DCH} \geqslant 8$ DCH cells, as a function of both the charge measured by LYSO detector and the TOF, respectively for the 90° (Fig. 2a) and 60° (Fig. 2b) set-up configurations. Fig. 2a includes also the events acquired with the heterogeneous target configuration. Following the analysis strategy already adopted in Rucinski et al. [30], the $N_{DCH} \geqslant 8$ DCH selection criteria was used to identify the secondary charged particles produced by the ^{16}O beam, which were subsequently used for

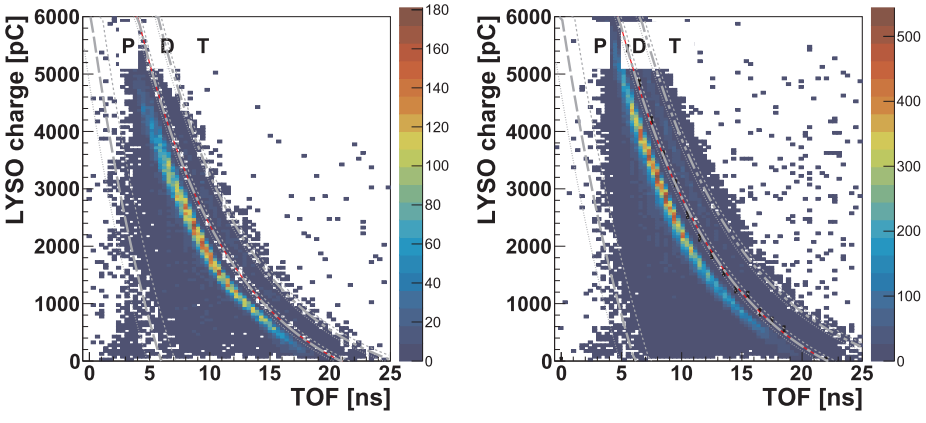

a ^{16}O, 90° configuration b ^{16}O, 60° configuration

Fig. 2. The secondary proton (p), deuteron (d), triton (t) and electron populations produced by ^{16}O beam in the PMMA as a function of TOF and LYSO charge measured in the 90° (a) and 60° (b) angular configurations. Dashed, dashed-dotted, dashed-dotted-dotted lines show how the electrons, p, d, and t were distinguished (note logarithmic scale). The systematic uncertainty relative to the PID procedure was estimated by shifting the separation lines as explained in detail in the text. The p, d, and t yields and energy spectra were calculated using the PID bold dashed lines shown on each plot. Panel (c) illustrates 8–9 ns TOF slice of the 60° distribution from panel (b). p distribution is fit with Gaussian function. d distribution is visible as a characteristic peak located to the right from the proton peak.

the emission profile reconstruction, and for the energy spectrum and yield measurements. In Fig. 2a and b the identification bands are built out of the charge vs TOF distributions, allowing to distinguish three different populations relative to protons (p), deuterons (d) and tritons (t). The population of events with TOF ~3.5 ns and energies up to few MeV/u is related to the electrons interacting with the LYSO detector, as verified using MC simulation studies.

The particle identification was performed exploiting the time and charge information of Fig. 2a, b and the algorithms already described in Mattei et al. [20], Rucinski et al. [30]. As the LYSO crystals have different light response to particles of same energy and type, due to the different optical coupling to the PMT and manufacturing, the DCH information was used to track each fragment impinging point on the different crystals, and to individually account for the charge measured in each crystal.

The dominant proton population clearly visible in the charge versus TOF distributions (Fig. 2a, b) was modeled with a double exponential function for each LYSO crystal separately. Such functions were used to adjust each LYSO crystal response to the reference one, as already described in [20]. Once equalized, the curves given by the minimum between the p and d, and d and t populations were modeled using a double exponential function and were taken as borders between regions populated by different particles (bold lines). The points of minimum between the two nearby populations have been obtained from the LYSO charge distribution in slice of given TOF. Fig. 2c shows for example the LYSO charge distribution for 8 ns ⩽ TOF ⩽ 9 ns in the 60° configuration.

The systematic uncertainty on the PID selection accounting for the underlying background contribution from neighboring populations was computed shifting the fitted functions (bold lines) in order to account for the limited precision on the measurement of the minimum values. The values were shifted ± 1σ (obtained from the charge distribution fit) and the corresponding dash-dotted lines were computed and used to re-evaluate the corresponding particle species yields. The electron separation, instead, was performed and optimized exploiting directly the information obtained from the MC simulations.

The raw number of detected secondary particles (p + d + t) is equal to $N_{ion} = 3.3 \times 10^4$ and $N_{ion} = 1.1 \times 10^5$ for the 90° and 60° configurations respectively (Fig. 2a and b). The raw population of detected secondary p, d, and t is divided as follows: about 91% (88%), 7% (11%), and 1% (2%) of the fragments are respectively p, d and t at 90° (60°) with respect to the incoming beam direction. These data were obtained with a corresponding total number $N_{ion} = 6.5 \times 10^9$ of incoming primary ^{16}O ions (including the heterogeneous target) in the 90° configuration, and $N_{ion} = 3.6 \times 10^9$ in the 60° configuration (see Table 1). These numbers enable a rough estimation of secondary particle yields of which the detailed calculation and the uncertainty considerations are given in Section 3.1.

3. Results

3.1. Yield and efficiency evaluation

In order to provide the *production* yields of p and d and of p, d and t respectively for the 90° and 60° angular configurations, when starting from the detected tracks, dedicated MC simulations were needed to compute and properly account for the experimental set-up detection efficiency.

Following the strategy already documented elsewhere [27,21,20,30], the differential production rate of charged secondary p, d and t fragments (measured at 90° and 60°, normalized to the number of primary ions, the total solid angle and integrated over the full target length as well as the detected spectrum of kinetic energy) has been computed accordingly to:

$$\Phi_{p,d,t} = \frac{dN_{p,d,t}}{N_{ion} d\Omega} = \frac{1}{4\pi} \frac{1}{N_{ion}\, \epsilon_{DT}} \sum_{E_{kin}^{Det}} \sum_{z} \frac{N_{p,d,t}(E_{kin}^{Det}, z)}{\epsilon_{p,d,t}(E_{kin}^{Det}, z)}, \quad (1)$$

where $N_{p,d,t}(E_{kin}^{Det}, z)$ is the number of detected p, d and t. N_{ion} is the number of primary ^{16}O ions impinging on the PMMA target. ϵ_{DT} is the dead time (DT) efficiency, and $\epsilon_{p,d,t}(E_{kin}^{Det}, z)$ is the total detection efficiency computed as a function of the production point (z) and of the kinetic energy (E_{kin}^{Det}) of secondary particles.

The dead time efficiency was introduced in order to account (i) for the loss in incoming ions counting due to the length of the trigger digital signal and (ii) for the dead time induced by the VME-based DAQ system [21,30]. Both effects are functions of the beam rate and were accounted for when computing the yields using Eq. (1) with ϵ_{DT} values computed specifically for each run, beam energy and angular configuration, allowing to obtain the correct number of ions impinging on the PMMA target. The DT efficiency was computed using the VME scaler information and is defined as $\epsilon_{DT} = N_{TrAcq}/N_{TrTot}$, where N_{TrAcq} is the number of trigger signals acquired by the DAQ system, and N_{TrTot} is the total number of generated trigger signals. The measured ϵ_{DT} values ranged from 55% to 80%. The correction factors, and their systematic uncertainties, used to account for the trigger signal length were obtained using dedicated, in-house implemented MC simulations of the beam time structure, as described in detail in Mattei et al. [21], and are varying in the 1.04–1.28 range.

The total detection efficiency $\epsilon_{p,d,t}(E_{kin}^{Det}, z)$ of secondary particles was computed from a MC simulation in which p, d and t fragments were directly generated inside the PMMA assuming an isotropic angular distribution, flat spatial and energy distributions. and counting the number of particles detected by LTS, DCH and LYSO in these conditions. In this way it was possible to obtain efficiency results that are independent from the FLUKA secondary production models and that covers all the energy and position phase space relative to the data distribution. The efficiency $\epsilon_{p,d,t}(E_{kin}^{Det}, z)$ is defined accordingly to Eq. (2) as:

$$\epsilon_{p,d,t}(E_{kin}^{Det}, z) = \frac{N^{det}(E_{kin}^{Det}, z)}{N^{gen}(E_{kin}^{Det}, z)} \quad (2)$$

where N^{det} and N^{gen} are respectively the number of detected and generated particles in the E_{kin}^{Det}, z bin.

An example of the total p detection efficiency map $\epsilon_p(E_{kin}^{Det}, z)$ is shown in Fig. 3b for the 90° set-up. The p efficiency maps are the same as those used in Rucinski et al. [30] when studying the ^{12}C and ^{4}He fragmentation, as they are independent of the production model and are accounting only for the p interactions with the target in their exit path towards the detector.

The efficiency maps $\epsilon_d(E_{kin}^{Det}, z)$ and $\epsilon_t(E_{kin}^{Det}, z)$ were computed, in addition, to study the d and t production from the ^{16}O beam interactions. The efficiency maps for p, d and t at 90° and 60° configurations are documented in the Supplementary material.

The efficiency map was computed using equally spaced intervals in the z and E_{kin}^{Det} variables (5 mm and 10 MeV respectively), and the systematic uncertainty was assessed using two different analysis methods and comparing the results [30].

The definition of $\epsilon_{p,d,t}(E_{kin}^{Det}, z)$ takes into account not only the LTS, DCH, LYSO detector efficiencies, but also the geometrical acceptance and the possible fragment absorption within the PMMA itself, and hence depends on the secondary particle production point in PMMA both along the longitudinal (z) and lateral (x) directions. The efficiency modulation along the (z) direction is mainly due to the detector system geometrical acceptance and, for more energetic particles, is dominated by the geometrical acceptance of DCH-LYSO system (Fig. 3b: yellow stripe around z = −5 cm).

The efficiency dependence on the (x) production position, i.e. radial distance from the beam axis due to nonzero lateral beam size, is affected by the interactions of produced fragments (energy loss and multiple Coulomb scattering) with the PMMA along their exit path

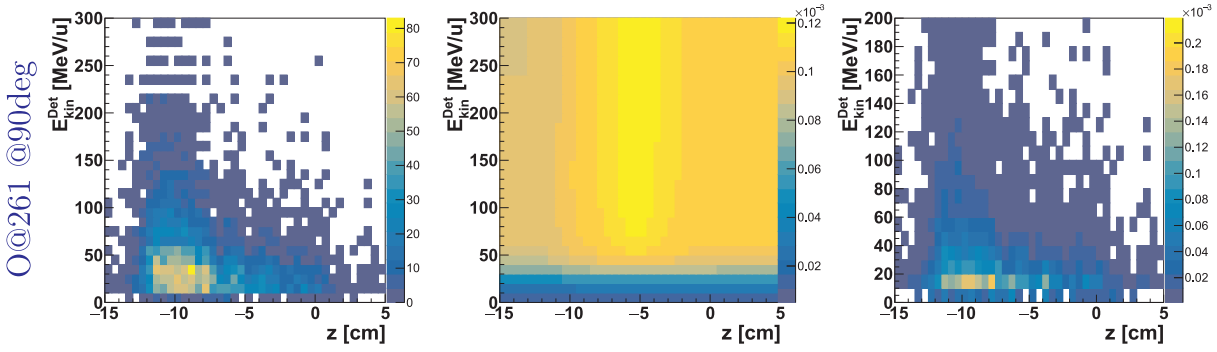

Fig. 3. (a) Number of secondary protons $N_p(E^{Det}_{kin}, z)$ produced by an ^{16}O beam of 260 MeV/u energy impinging on the heterogeneous target and detected by the DCH detector. No efficiency correction is applied. (b) Efficiency map $\epsilon_p(E^{Det}_{kin}, z)$ obtained from MC simulations. For details regarding the efficiency definition and calculation, please see the text. (c) Secondary proton yield $\Phi_p(E^{Det}_{kin}, z)$ as computed following the definition detailed in the text, accounting for the efficiency shown in (b). The (a–c) distributions are showing the results obtained in the 90° set-up configuration. The data are shown as a function of the detected kinetic energy (E^{Det}_{kin}) and reconstructed production point (z).

towards the detector. Fig. 3b shows that depending on the secondary particle production point along the (x) direction, the probability to escape the PMMA target is smaller for less energetic particles, namely for $E^{Prod}_{kin} < 50$ MeV as shown in Fig. 3b (blue area).

The yields of secondary p, d and t fragments were calculated accordingly to Eq. (1). The $\Phi_{p,d,t}(E^{Det}_{kin}, z)$ measurements can be used as an input for the validation of MC models used for the production of secondary charged particles in matter, and hence for PT monitoring applications when evaluating the fragments' statistics available in clinical conditions.

Fig. 3a–c are respectively showing the number N_p of detected protons, efficiency ϵ_p and final yield Φ_p distributions obtained when studying the 260 MeV/u ^{16}O beam interactions with the heterogeneous target. The complete set of results obtained for all the secondary p, d and t production, for all energies, target types and set-up configurations are collected in the Supplementary material, whereas the integrated yields are listed in Table 2 and illustrated in Fig. 3a as a function of the primary beam energy per nucleon for both angular set-up configurations. Single charged secondary particles with detected kinetic energy greater than the kinetic energy of primary ^{16}O beam can be observed for all beam energies (see Fig. 3a and Supplementary material), and are more abundant at 60° with respect to 90°.

The results obtained studying the ^{16}O beam interactions are superimposed, in Fig. 4, to the p yields measured using ^{4}He and ^{12}C beams as reported in Rucinski et al. [30]. The proton production Φ_p is dominant, in both angular configurations, with respect to the deuteron Φ_d and triton Φ_t contributions at all energies. The yield of secondary particles produced in the target increases with the energy of the primary beam, i.e. with its range, as the secondary particles are essentially the products of the projectile fragmentation, and is nearly one order of magnitude greater at 60° with respect to 90° measurements.

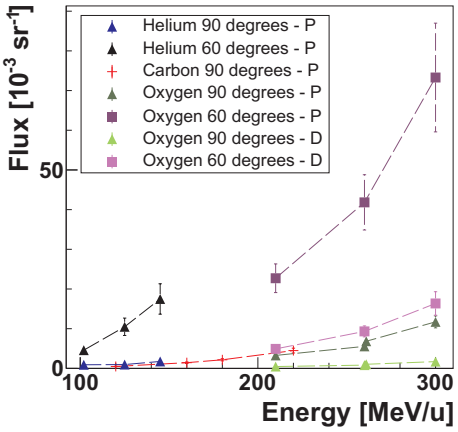

Fig. 4. The secondary proton Φ_p and deuteron Φ_d yields measured with the detector positioned at 90° and 60° with respect to the incoming beam direction. Fragments were produced by the primary ^{16}O beam (red markers) of different kinetic energy impinging on a PMMA target. Closed and open markers are used to distinguish secondary p and d production. To distinguish production at 90 and 60°, square and triangle markers are used. Charged secondary production from ^{4}He, ^{12}C [30], and ^{16}O beams was marked with blue, black and red. The total uncertainty shown in the plot is the sum in quadrature of the statistical and systematic contributions. (For interpretation of the references to colour in this figure legend, the reader is referred to the web version of this article.)

The secondary proton and deuteron yields measured studying the 260 MeV/u ^{16}O beam interactions with the heterogeneous PMMA target are marked in Table 2 by an asterisk, and are in agreement, within the

Table 2
The secondary proton Φ_p, deuteron Φ_d and triton Φ_t yields measured with the detector positioned at $\theta = 90°$ and 60° with respect to the incoming beam direction. Fragments were produced by the primary ^{16}O beam with different kinetic energy impinging on a PMMA target. The measurements performed with the heterogeneous PMMA target are marked with an asterisk.

Beam	θ	Energy [MeV/u]	$\Phi_p \pm \sigma_{stat} \pm \sigma_{sys}$ [10^{-3} sr^{-1}]	$\Phi_d \pm \sigma_{stat} \pm \sigma_{sys}$ [10^{-3} sr^{-1}]	$\Phi_t \pm \sigma_{stat} \pm \sigma_{(sys}$ [10^{-3} sr^{-1}]
^{16}O	90°	210	3.25 ± 0.06 ± 0.41	0.47 ± 0.03 ± 0.22	–
		260	5.48 ± 0.12 ± 0.68	0.91 ± 0.06 ± 0.38	–
		260*	6.73 ± 0.11 ± 0.74	1.18 ± 0.06 ± 0.49	–
		300	11.60 ± 0.11 ± 1.41	1.84 ± 0.06 ± 0.77	–
	60°	210	22.86 ± 0.23 ± 3.44	4.91 ± 0.13 ± 0.57	1.69 ± 0.15 ± 0.24
		260	42.21 ± 0.36 ± 6.60	9.23 ± 0.21 ± 1.00	3.87 ± 0.26 ± 0.46
		300	74.18 ± 0.40 ± 13.02	16.07 ± 0.23 ± 1.98	11.75 ± 0.40 ± 1.47

uncertainty, with the measurement performed with a homogeneous target. This result is expected, since the secondary particle production occurs mainly in the PMMA target material.

The uncertainty listed in Table 2 is the statistical σ_{stat} and systematic σ_{sys} contribution. The total relative uncertainty ranges (see Fig. 4) are 11–18% for p, 11–46% for d, and 13–17% for t (the t results are significantly different from zero only at 60°) and are dominated by the systematic uncertainty contribution.

The relative statistical uncertainty on yield calculation is dominated by the uncertainty on the number of detected charged secondary particles, that depends on the beam energy, secondary particle type and angular set-up configuration. This uncertainty ranges from 0.5% for secondary p to 9% for secondary t (the yield of secondary t at 90° was consistent with zero and hence not reported or considered in the results). The contributions to the statistical uncertainty from the MC detection efficiency evaluation and the number of primary ions are negligible.

The relative systematic uncertainty on the yield calculation is dominated by the uncertainty in the computation of the total detection efficiency map. The relative yield semi-dispersion computed using the two different efficiency map computation methods, which were described in detail in Rucinski et al. [30] and implement different MC simulation samples and extrapolation algorithms in the low energy region, ranges from 2% to 46%. The large variations occur in the low energy part of the spectrum and are reflecting the inaccuracy in the energy loss estimation and amount of absorption near the threshold in this region. The systematic uncertainty on the efficiency calculation introduced using an isotropic angular distribution has been assumed negligible with respect to the other contributions. When studying the efficiency in bins of E_{kin}^{Det} and z, highly correlated with the emission angle, the remaining dependence on the angle is largely reduced. Furthermore, the particles intercepted by the detector have similar production angles due to the small detector acceptance (within ± 2° with respect to the selected direction). The PID systematic uncertainty, i.e. the systematic uncertainty related to the particle mis-identification, is below 1.5% for p, but ranges from 7% to 15% for d and t. Fig. 2 shows the reference, soft and hard PID selection bands used to calculate the uncertainty on the secondary particle yield. The systematic uncertainty related to the estimation of the raw number of primary ions N_{ion} was assessed with two methods: (i) using a dedicated MC simulation and (ii) using the other (PET) detectors that were part of the full experimental set-up, as described in detail in Rucinski et al. [30], Mattei et al. [21]. The corresponding uncertainties are in the 3–5% and 3–4.5% range, respectively. The systematic uncertainty contributions related to DCH selection criteria (computed by changing the selection criteria as follows: $N_{DCH} \geqslant 7$ or $N_{DCH} \geqslant 9$) as well as dead time efficiency are negligible.

3.2. Energy spectra

Fig. 5 shows energy spectra of the detected secondary particles, i.e. the p, d and t production yields as a function of secondary particle detection energy (E_{kin}^{Det}). The results obtained studying the collisions of ^{16}O beams with 210, 260 and 300 MeV/u kinetic energy are shown. The first row of plots shows the results obtained with the detector at 90° with respect to incoming beam direction, while the second row shows the results at 60°.

The yields increase and the energy spectrum widens when the ^{16}O beam energy (and range) increases. In particular, with increasing ^{16}O beam energy, the produced fragments are more energetic, and a larger fraction of them can escape the target/patient and reach the detectors. The yield integrated over the energy spectrum is equal to the total yield reported in Table 2 and Fig. 4.

The energy spectra shown in Fig. 5 were obtained by integrating the two dimensional $\Phi_{p,d,t}(E_{kin}^{Det}, z)$ distributions (e.g. Fig. 3c) over the PMMA target length (z). The uncertainty on the secondary particle yield $\Phi_{p,d,t}(E_{kin}^{Det}, z)$ increases when the secondary particle detection energy E_{kin}^{Det} decreases (first bins of Fig. 5) and the mass number increases, mainly due to the systematic uncertainty contribution from the total detection efficiency map evaluation (see Sec. 3.1).

When computing E_{kin}^{Prod} using E_{kin}^{Det} information, one has to account for the uncertainty on the actual production point of the secondary particle in the PMMA. Such point varies due to the nonzero Oxygen beam size that increases very slightly with the beam path inside the PMMA, due to the multiple Coulomb scattering. The different distances that the fragment has to travel inside the target in its exit path towards the detector results in the uncertainty documented in Rucinski et al. [30]Fig. 5. The secondary particles with a production energy $E_{kin}^{Prod} > 60$ MeV are considered as the most interesting for monitoring purposes [2,30], as they have enough energy to escape the patient, even in the case of deep seated tumors.

3.3. Emission profiles

The secondary particle emission profiles along the longitudinal direction were reconstructed by back-tracking the detected secondary particles towards the PMMA target [9,27,30]. The profiles obtained with ^{16}O beams of 210, 260 and 300 MeV/u are shown in Fig. 6b and c for 90° and 60° set-up configurations, respectively. Fig. 6a shows an overlap of the depth dose distribution profile of an ^{16}O beam of 260 MeV/u in the PMMA as obtained from FLUKA simulations superimposed to the detected charged secondary emission profile.

The shape of the charged secondary emission profile shown in Fig. 6 varies as a function of the ^{16}O primary beam energy with characteristics that are similar to what was already observed studying the interactions of ^{4}He and ^{12}C beams. PMMA targets of different length, determined by the ^{16}O beam energy (see Table 1), were used for the measurements: Fig. 6a and b demonstrate the clear correlation between the rising edge of the profile and the target length that easily allows the identification of the PMMA entrance face position. The overall shape of the emission profile can be correlated to the range of the primary beam as discussed in Piersanti et al. [27]. Some characteristic features of the shape (e.g. the slope of the emission's falling edge) depend on the choice of primary ion type, and have to be calibrated to fully exploit this range monitoring technique in the clinical case. Such profile could be used for range monitoring purposes in particle therapy with ^{16}O beams in the same way as with ^{4}He and ^{12}C beams, as presented in Piersanti et al. [27], Mattei et al. [20], Rucinski et al. [30].

4. Discussion

The measured proton, deuteron and triton yields produced by primary ^{16}O beams impinging on a thick target indicate that these particles can be potentially considered as candidates to be exploited for primary beam range monitoring applications. The yields range from 0.5 to 74.2×10^{-3} sr^{-1} per primary ^{16}O ion, and depend on the charged secondary particle type (proton, deuteron, triton), the emission angle and the primary ^{16}O beam energy. The total fractional uncertainty on the measured yields of secondary protons is in range 11–18%. At large angle with respect to the incoming beam direction, the charged fragments production is clearly dominated by the proton contribution. The energy spectra were measured using the TOF technique and show that at 60° a significant amount of fragments are produced with relatively large kinetic energy (larger than 100 MeV/u).

The charged secondary particle yields produced by ^{16}O beams shown in Fig. 4 are, as expected, higher than the yields produced with an ion beam of lower Z (^{4}He and ^{12}C). The deuteron yield produced by ^{16}O beams is comparable to the proton yield produced by the ^{4}He beam for both 60° and 90° set-up configurations.

Fig. 7 illustrates that the beam range as well as the target heterogeneities can be identified using the charged secondary emission profile, similarly to what was reported by Gaa et al. [8] exploiting both PG

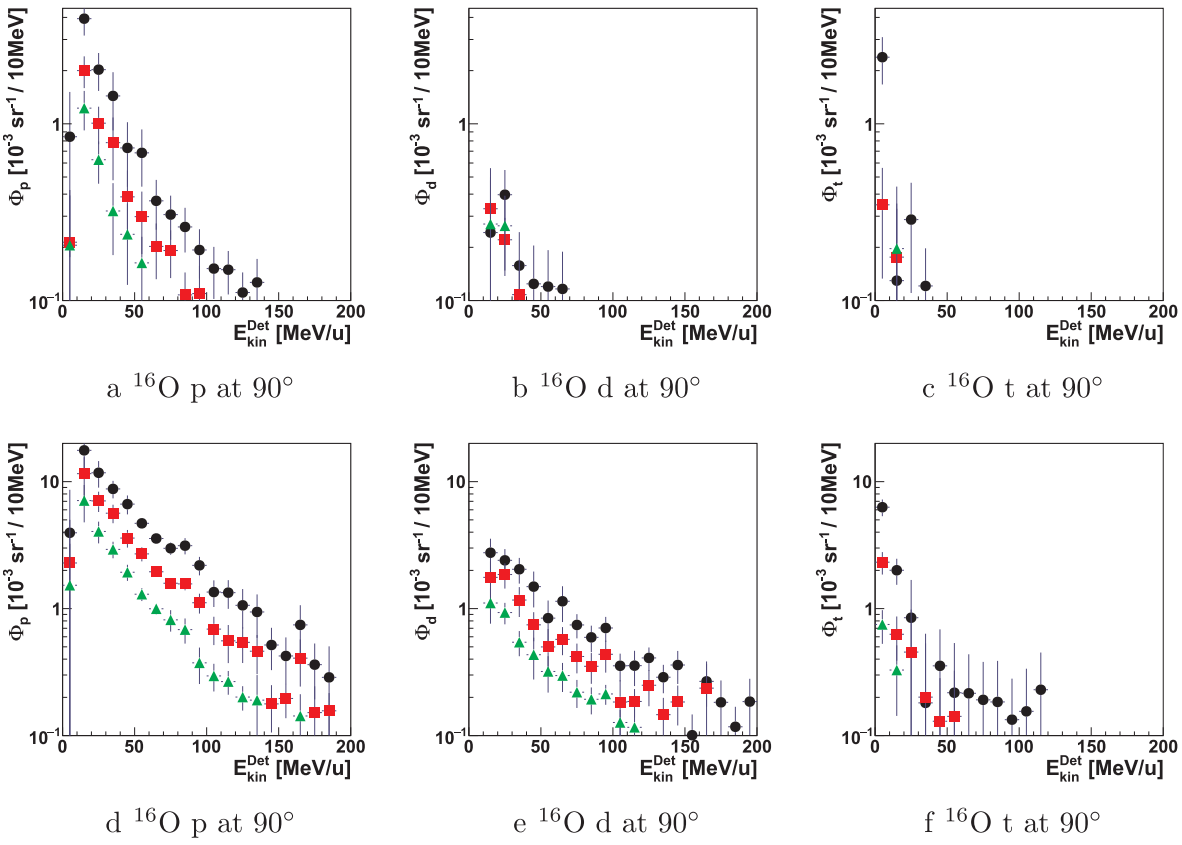

Fig. 5. The secondary proton (a,c), deuteron (b,d) and triton (e) yields produced in the interaction of ^{16}O beams of 210 MeV/u (green), 260 MeV/u (red), and 300 MeV/u (black) energy as a function of the detected kinetic energy E^{Det}_{kin} of the secondary particles. The energy spectra in plots (a,b) and (c,d,e) were measured with the detector placed respectively at 90° and 60° with respect to the incoming beam direction. The total uncertainty that is shown is the sum in quadrature of the statistical and systematic contributions (see Table 2). (For interpretation of the references to colour in this figure legend, the reader is referred to the web version of this article.)

and charged secondary radiation. The emission shape was obtained from a data sample collected using the ^{16}O beam at 260 MeV impinging on a heterogeneous target consisting of four PMMA blocks with length 5 cm, 1 cm, 1.5 cm and 2.65 cm, separated by three 1 cm long air gaps. Fig. 7 was obtained with 12442 secondary proton tracks. The statistical uncertainty is illustrated with error bars. The correlation between the target position and the secondary charged fragments production points is shown.

A method to deconvolve the interactions undergone by the fragments inside the target material (absorption, multiple scattering), as well as their different production rates due to different target densities, is needed in order to assess the final accuracy achievable when trying to identify the target inhomogeneities in PT treatments applications. The proposed set-up was designed to obtain a characterization of the yields of charged secondary particles. An alternative approach for the more complex clinical case was proposed and discussed in Battistoni et al. [3], Traini et al. [37]. In the new set-up the drift chamber is replaced by a self-triggering tracking detector based on scintillating fibers. This solution is a subject of further, ongoing studies which will be performed with anthropomorphic phantoms and patients undergoing ^{12}C therapy in CNAO. Aim of such studies is to finally assess the feasibility of the charged secondary technique, assessing the actual resolution on the BP position, in a clinical case scenario.

5. Conclusions

Secondary radiation measurements for particle therapy applications is a series of manuscripts characterizing the secondary radiation produced by ^{4}He, ^{12}C, and ^{16}O beams.

This paper reports on the data analysis performed to characterize the charged secondary radiation produced in a thick PMMA target irradiated with ^{16}O beams with energies of interest for charged PT applications (namely 210, 260, and 300 MeV/u). The experimental set-up included a PMMA target, two plastic scintillators, a drift chamber and four LYSO crystals arranged in a single detector, and allowed to perform the production measurements in two different angular configurations (90° and 60° with respect to the primary beam direction). The collected information was used to estimate charged secondary particle yields, energy spectra and emission profiles accounting for the detection and geometrical efficiencies using MC simulations. Such information is consistent and complementary to published data obtained with ^{4}He and ^{12}C beams.

The presented results are an essential piece of information when trying to assess the performance of range monitoring detectors for charged particle therapy. The obtained yield characterization supports the feasibility of charged PT online monitoring techniques exploiting the reconstructed emission profile of charged fragments. The actual accuracy attainable in monitoring the BP position in heterogeneous target conditions as in the clinical case is beyond the scope of this manuscript, and is discussed in detail in other publications [28,37,3].

Acknowledgements

We would like to sincerely thank Marco Magi (SBAI Department) for his valuable effort in the construction of several mechanical parts of the experimental set-up. This work has been partly supported by the “Museo storico della Fisica e Centro di studi e ricerche Enrico Fermi”. The access to the test beam at the Heidelberg Ion-beam Therapy center

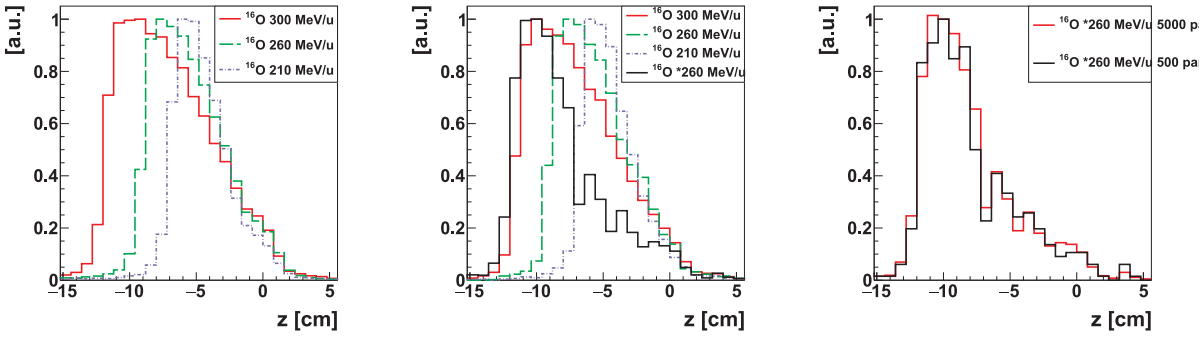

a ^{16}O beam, 60°configuration. b ^{16}O beam, 90°configuration. c ^{16}O beam, 90°configuration.

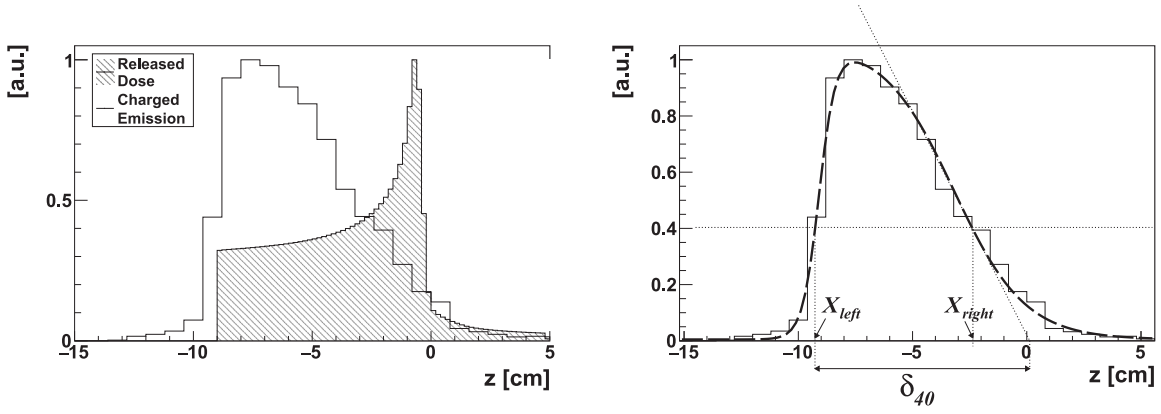

d ^{16}O beam at 260 MeV/u, 90°configuration. e ^{16}O beam at 260 MeV/u, 90°configuration.

Fig. 6. Longitudinal charged secondary emission profiles reconstructed by back-tracking the secondary particles produced in the interaction of ^{16}O beams of 300, 260, and 210 MeV/u energy with the homogeneous target. The results obtained with the detector placed at 90° (a-b) and 60° (c) with respect to the incoming beam direction, are shown. The PMMA entrance face positions are respectively − 11.7, −9.0 and − 6.7 cm. Panel a) illustrates the Dose Release of an ^{16}O beam at 260 MeV/u in the PMMA target and the corresponding expected charged particles emission, based on MC simulations.

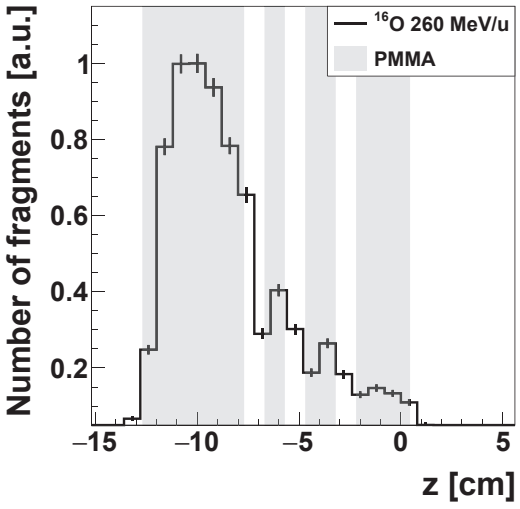

Fig. 7. The charged secondary emission shape produced by a 260 MeV/u ^{16}O beam (8.4 cm range in PMMA) impinging on a heterogeneous target consisting of four PMMA slabs (gray regions) with total length of 10 cm, separated by 1 cm long air gaps. Details on the heterogeneous target set-up and the relative results are given in Sections 2.1 and 3.1 respectively.

was granted by the ULICE European program. We are indebted to Prof. Dr. Thomas Haberer and Dr. Stephan Brons for having encouraged this measurement campaign, which was realized thanks to their support and to the help of the whole HIT staff.

Appendix A. Supplementary data

Supplementary data associated with this article can be found, in the online version, at https://doi.org/10.1016/j.ejmp.2019.06.001.

References

[1] Abou-Haidar Z, et al. Performance of upstream interaction region detectors for the FIRST experiment at GSI. J Instrum 2012;7(02):P02006. URL:http://stacks.iop.org/1748-0221/7/i=02/a=P02006.
[2] Agodi C, et al. Charged particle's flux measurement from PMMA irradiated by 80 MeV/u carbon ion beam. Phys Med Biol 2012;57(18):5667. URL:http://stacks.iop.org/0031-9155/57/i=18/a=5667.
[3] Battistoni G, et al. Design of a tracking device for on-line dose monitoring in hadrontherapy. Nucl Instrum Methods Phys Res Sect A 2017;845:679–83. https://doi.org/10.1016/j.nima.2016.05.095.
[4] Bauer J, Unholtz D, Sommerer F, Kurz C, Haberer T, Herfarth K, Welzel T, Combs SE, Debus J, Parodi K. Implementation and initial clinical experience of offline pet/ct-based verification of scanned carbon ion treatment. Radiother Oncol 2013;107(2):218–26.
[5] Boehlen T, et al. The FLUKA code: developments and challenges for high energy and medical applications. Nucl Data Sheets 2014;120:211–4.
[6] Durante M, Orecchia R, Loeffler JS. Charged-particle therapy in cancer: clinical uses and future perspectives. Nat Rev Clin Oncol 2017;14. https://doi.org/10.1038/nrclinonc.2017.30. 483 EP –.
[7] Ferrari A, et al. FLUKA: A multi-particle transport code (program version 2005) Technical Report CERN-2005-10, INFN/TC 05/11, SLAC-R-773 Geneva; 2005.
[8] Gaa T, et al. Visualization of air and metal inhomogeneities in phantoms irradiated by carbon ion beams using prompt secondary ions. Physica Med 2017;38:140–7. URL:http://www.sciencedirect.com/science/article/pii/S1120179717301709.
[9] Gwosch K, et al. Non-invasive monitoring of therapeutic carbon ion beams in a

homogeneous phantom by tracking of secondary ions. Phys Med Biol 2013;58:3755.
[10] Henriquet P, et al. Interaction vertex imaging (IVI) for carbon ion therapy monitoring: a feasibility study. Phys Med Biol 2012;57:4655–69.
[11] Knopf AC, Lomax A. vivo proton range verification: a review. Phys Med Biol 2013;58(15):R131–60.
[12] Kraan AC. Range verification methods in particle therapy: underlying physics and monte carlo modeling. Front Oncol 2015;5:150.
[13] Kraan AC, et al. First tests for an online treatment monitoring system with in-beam PET for proton therapy. J Instrum 2014;10.
[14] Krimmer J, et al. Prompt-gamma monitoring in hadrontherapy: a review. Nucl Instrum Methods Phys Res Sect A 2017. URL:http://www.sciencedirect.com/science/article/pii/S0168900217308380.
[15] Kurz C, et al. First experimental-based characterization of oxygen ion beam depth dose distributions at the heidelberg ion-beam therapy center. Phys Med Biol 2012;57(15):5017. URL:http://stacks.iop.org/0031-9155/57/i=15/a=5017.
[16] Mairani A, et al. Biologically optimized helium ion plans: calculation approach and its in vitro validation. Phys Med Biol 2016;61(11):4283. URL:http://stacks.iop.org/0031-9155/61/i=11/a=4283.
[17] Mairani A, et al. Data-driven RBE parameterization for helium ion beams. Phys Med Biol 2016;61(2):888. URL:http://stacks.iop.org/0031-9155/61/i=2/a=888.
[18] Marafini M, et al. Secondary radiation measurements for particle therapy applications: nuclear fragmentation produced by 4He ion beams in a PMMA target. Phys Med Biol 2017;62(4):1291. URL:http://stacks.iop.org/0031-9155/62/i=4/a=1291.
[19] Matsufuji N, et al. Spatial fragment distribution from a therapeutic pencil-like carbon beam in water. Phys Med Biol 2005;50(14):3393. URL:http://stacks.iop.org/0031-9155/50/i=14/a=014.
[20] Mattei I, et al. Addendum: measurement of charged particle yields from PMMA irradiated by a 220 MeV/u 12C beam. Phys Med Biol 2017;62(21):8483. URL:http://stacks.iop.org/0031-9155/62/i=21/a=8483.
[21] Mattei I, et al. Secondary radiation measurements for particle therapy applications: prompt photons produced by 4He, 12C and 16O ion beams in a PMMA target. Phys Med Biol 2017;62(4):1438. URL:http://stacks.iop.org/0031-9155/62/i=4/a=1438.
[22] Muraro S, et al. Monitoring of hadrontherapy treatments by means of charged particle detection. Front Oncol 2016;6:177. URL:https://www.frontiersin.org/article/10.3389/fonc.2016.00177.
[23] Parodi K. Vision 20/20: positron emission tomography in radiation therapy planning, delivery, and monitoring. Med Phys 2015;42(12):7153.
[24] Parodi K, Bortfeld T, Haberer T. Comparison between in-beam and offline positron emission tomography imaging of proton and carbon ion therapeutic irradiation at synchrotron- and cyclotron-based facilities. Int J Radiat Oncol Biol Phys 2008;71(3):945–56.
[25] Parodi K, Enghardt W. Potential application of PET in quality assurance of proton therapy. Phys Med Biol 2000;45(11):N151. URL:http://stacks.iop.org/0031-9155/45/i=11/a=403.
[26] Pennazio F, et al. Carbon ions beam therapy monitoring with the inside in-beam pet. Phys Med Biol 2018. URL:http://iopscience.iop.org/10.1088/1361-6560/aacab8.
[27] Piersanti L, et al. Measurement of charged particle yields from PMMA irradiated by a 220 MeV/u 12 C beam. Phys Med Biol 2014;59(7):1857. URL:http://stacks.iop.org/0031-9155/59/i=7/a=1857.
[28] Reinhart A, et al. Three dimensional reconstruction of therapeutic carbon ion beams in phantoms using single secondary ion tracks. Phys Med Biol 2017;62(12):4884–96.
[29] Richter C, et al. First clinical application of a prompt gamma based in vivo proton range verification system. Radiother Oncol 2016;118(2):232–7. URL:http://www.sciencedirect.com/science/article/pii/S0167814016000074.
[30] Rucinski A, et al. Secondary radiation measurements for particle therapy applications: charged particles produced by 4 he and 12 c ion beams in a pmma target at large angle. Phys Med Biol 2018;63(5):055018. URL:http://stacks.iop.org/0031-9155/63/i=5/a=055018.
[31] Salvador S, Colin J, Cussol D, Divay C, Fontbonne JM, Labalme M. Cross section measurements for production of positron emitters for pet imaging in carbon therapy. Phys Rev C 2017;95:044607. URL:https://link.aps.org/doi/10.1103/PhysRevC.95.044607.
[32] Seravalli E, Robert C, Bauer J, Stichelbaut F, Kurz C, Smeets J, Ty CVN, Schaart DR, Buvat I, Parodi K, Verhaegen F. Monte carlo calculations of positron emitter yields in proton radiotherapy. Phys Med Biol 2012;57(6):1659–73. https://doi.org/10.1088/0031-9155/57/6/1659.
[33] Sokol O, et al. Oxygen beams for therapy: advanced biological treatment planning and experimental verification. Phys Med Biol 2017;62(19):7798. URL:http://stacks.iop.org/0031-9155/62/i=19/a=7798.
[34] Sportelli G, et al. First full-beam PET acquisitions in proton therapy with a modular dual-head dedicated system. Phys Med Biol 2014;59(1):43. URL:http://stacks.iop.org/0031-9155/59/i=1/a=43.
[35] Tommasino F, Durante M. Proton Radiobiol Cancers (Basel) 2015;7(1):353–81.
[36] Tommasino F, Scifoni E, Durante M. New ions for therapy. Int J Particle Ther 2015;2(3):428–38. https://doi.org/10.14338/IJPT-15-00027.1.
[37] Traini G, et al. Design of a new tracking device for on-line beam range monitor in carbon therapy. Physica Med 2017;34:18–27.
[38] Verburg J, et al. Su-f-601-2: clinical translation of prompt gamma-ray spectroscopy for in vivo proton range verification. Med Phys (Scientific Abstracts and Sessions) 2017;44(6):2721–3318. https://doi.org/10.1002/mp.12304.
[39] Xie Y, et al. Prompt gamma imaging for in vivo range verification of pencil beam scanning proton therapy. Int J Radiat Oncol Biol Phys 2017;99(1):210–8. https://doi.org/10.1016/j.ijrobp.2017.04.027.